

# Facile hyperpolarization chemistry for molecular imaging and metabolic tracking of [1-<sup>13</sup>C]pyruvate *in vivo*

Austin Browning,<sup>a</sup> Keilian McCulloch,<sup>a</sup> David Guarin Bedoya,<sup>b</sup> Carlos Dedesma,<sup>c</sup> Boyd M. Goodson,<sup>d</sup> Matthew S. Rosen,<sup>b</sup> Eduard Y. Chekmenev,<sup>e,f</sup>, Yi-Fen Yen,<sup>b</sup> Patrick TomHon\*<sup>c</sup> and Thomas Theis\*<sup>a,g,h</sup>

<sup>a</sup> Department of Chemistry, North Carolina State University, Raleigh, North Carolina 27695, United States

<sup>b</sup> Department of Radiology, Athinoula A. Martinos Center for Biomedical Imaging, Massachusetts General Hospital, Charlestown, Massachusetts, United States

<sup>c</sup> Vizma Life Sciences Inc., Chapel Hill, North Carolina 27514, United States

<sup>d</sup> School of Chemical & Biomolecular Sciences and Materials Technology Center, Southern Illinois University, Carbondale, Illinois 62901, United States

<sup>e</sup> Department of Chemistry, Integrative Bio-sciences (Ibio), Karmanos Cancer Institute (KCI), Wayne State University, Detroit, Michigan 48202, United States

<sup>f</sup> Russian Academy of Sciences, 119991 Moscow, Russia

<sup>g</sup> Department of Physics, North Carolina State University, Raleigh, North Carolina 27606, United States

<sup>h</sup> Joint UNC & NC State Department of Biomedical Engineering, North Carolina State University, Raleigh, North Carolina 27606, United States

## ABSTRACT

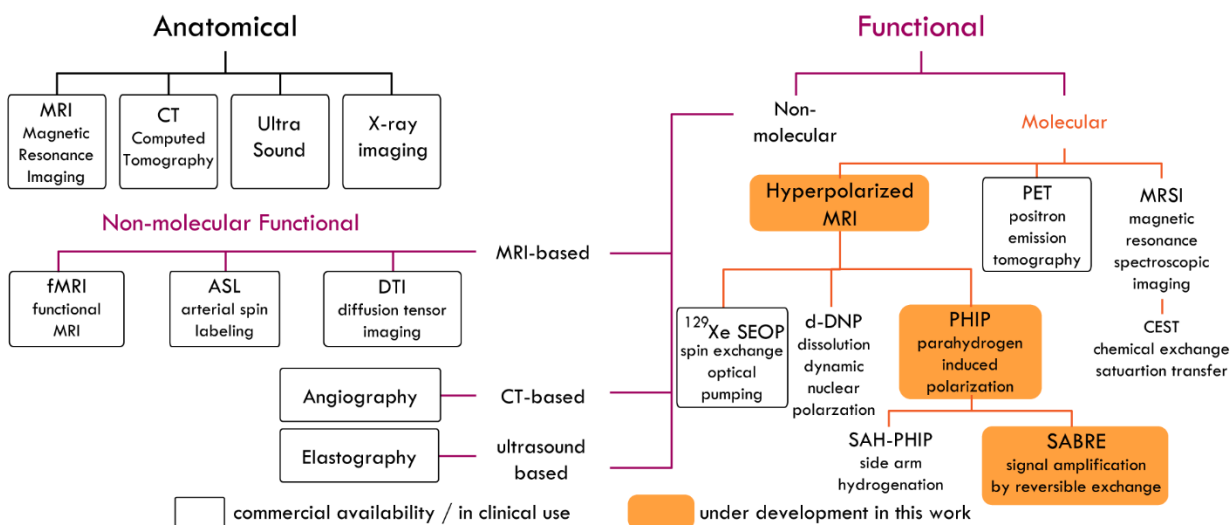
Hyperpolarization chemistry based on reversible exchange of parahydrogen, also known as Signal Amplification By Reversible Exchange (SABRE), is a particularly simple approach to attain high levels of nuclear spin hyperpolarization, which can enhance NMR and MRI signals by many orders of magnitude. SABRE has received significant attention in the scientific community since its inception because of its relative experimental simplicity and its broad applicability to a wide range of molecules, however *in vivo* detection of molecular probes hyperpolarized by SABRE has remained elusive. Here we describe the first demonstration of SABRE-hyperpolarized contrast detected *in vivo*, specifically using hyperpolarized [1-<sup>13</sup>C]pyruvate. A biocompatible formulation of hyperpolarized [1-<sup>13</sup>C]pyruvate was injected into healthy Sprague Dawley and Wistar rats, and metabolic conversion of pyruvate to lactate, alanine, pyruvate-hydrate, and bicarbonate was detected. Measurements were performed on the liver and kidney at 4.7 T via time-resolved spectroscopy and chemical-shift-resolved MRI. In addition, whole-body metabolic measurements

were obtained using a cryogen-free 1.5 T MRI system, illustrating the utility of combining lower-cost MRI systems with simple, low-cost hyperpolarization chemistry to develop scalable, next-generation molecular imaging.

## INTRODUCTION

Current medical imaging techniques fall in two broad categories, anatomical and functional imaging.<sup>1,2</sup> Anatomical imaging provides structural information, whereas functional imaging provides information about the mechanistic underpinnings of biological activity often unfolding on the molecular level.<sup>3-5</sup> As illustrated in Fig. 1A, there are many anatomical imaging methods used in clinical settings including Magnetic Resonance Imaging (MRI), ultrasound, x-ray, and computed tomography (CT).<sup>5</sup> MRI uses the large amounts of water and fat protons in the body to obtain high-resolution images of tissues and organs.<sup>6,7</sup> Ultrasound applies high-frequency acoustic waves to visualize the body's internal organs and is typically associated with lower resolution compared to MRI, but ultrasound stands out due to its speed and real-time imaging capabilities and because it is inexpensive and easy to deploy.<sup>8,9</sup> Simple x-rays have outstanding resolution for visualizing bone but have limited soft-tissue contrast.<sup>10-12</sup> Computed tomography (CT) uses multi-plane x-ray images processed via mathematical reconstruction algorithms and can give key insights to internal injuries and pathologies on its own, or when combined with iodine contrast agents.<sup>13,14</sup> MRI, ultrasound, x-ray, and CT all give high-precision structural contrast, and careful developments have been added over the years to extract functional information with these methods. Many existing functional imaging approaches can be thought of as off-shoots of the listed structural methods.

A) An overview of current imaging modalities, placing hyperpolarization chemistry in context



B) SABRE hyperpolarization chemistry

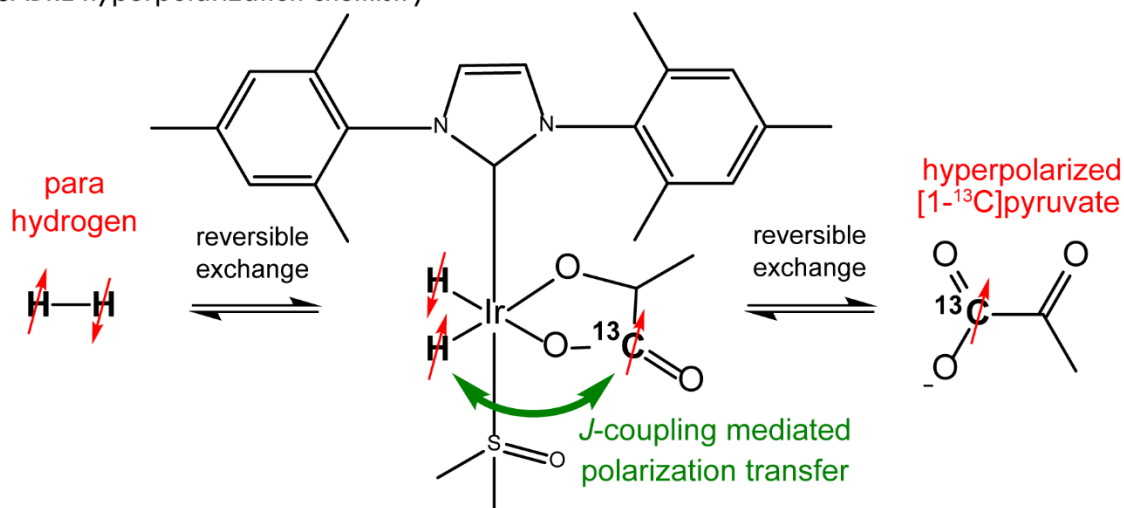


Figure 1. A) Illustration of the medical imaging landscape placing hyperpolarized imaging and specifically parahydrogen-driven SABRE hyperpolarization chemistry in broader context. The diagram does not exhaustively capture all medical imaging methods. The highlighting of methods that have “commercial availability” emphasizes the current methods that are used in clinics. Hyperpolarized MRI and SABRE as relevant to this work are highlighted in orange. B) SABRE hyperpolarization chemistry: Both parahydrogen and the  $[1-^{13}\text{C}]$ pyruvate substrate are in reversible exchange with the polarization transfer catalyst,  $[\text{IrH}_2(\text{IMes})(\text{DMSO})(\text{pyruvate})]$ . During the lifetime of the polarization-transfer complex that comprises the catalyst, the substrate, and parahydrogen (tens to hundreds of milliseconds), the polarization is transferred from the parahydrogen singlet state on the hydrides to the  $^{13}\text{C}$  nucleus in pyruvate transiently bound on the catalyst. Continuous exchange leads to hyperpolarization build-up on the free pyruvate in solution. This build-up process requires roughly 1.5 minutes to reach steady-state hyperpolarization.

These functional imaging methods can be broken down further into molecular and non-molecular functional imaging modalities. The non-molecular modalities typically employ subtle changes in the data acquisition and data reconstruction schemes to access functional information. MRI lends itself particularly well to this approach because MRI signals are strongly dependent on the exact sample composition and MRI sequences can be modified in a myriad of possible ways. Good examples include functional Magnetic Resonance Imaging (fMRI), which is sensitive to changes in blood oxygenation level,<sup>15-18</sup> Arterial spin labeling (ASL) that measures tissue perfusion via magnetic labeling of slices in the object that are subject to perfusion,<sup>19-21</sup> and Diffusion Tensor Imaging (DTI), which measures the three-dimensional diffusion of water as a function of spatial location.<sup>22,23</sup> Non-MRI functional imaging includes CT angiography using CT scans after injection of a dye to produce images of blood vessels and tissues,<sup>24</sup> and ultrasound elastography, which is sensitive to the stiffness of tissues because acoustic wave propagation depends on material stiffness and can be used to distinguish healthy from pathological tissue.<sup>25</sup> These non-molecular functional imaging methods are sensitive to blood flow and tissue activity but do not give insights into fundamental biological processes on the molecular level. Conversely, *molecular* functional imaging methods use biomarkers that directly report on biological function. The two predominant methods are Positron Emission Tomography (PET) and hyperpolarized MRI. PET has been translated all the way to clinical practice and uses radioactive tracers that are injected and detected via the emitted radiation.<sup>26,27</sup> PET has unrivaled sensitivity to picomolar concentrations of radiotracers and has revolutionized staging and monitoring response to treatment of many diseases, most notably various cancers. However, PET also has significant weaknesses, which include the use of ionizing radiation, limited spatial resolution, a requirement for large and sophisticated infrastructure, and a lack of sensitivity to chemical transformations. In contrast, Magnetic

Resonance (MR) techniques (exemplified by magnetic resonance spectroscopic imaging MRSI<sup>28-30</sup> or Chemical Exchange Saturation Transfer (CEST)<sup>31-33</sup>) are highly sensitive to small changes in molecular structure as reported by the chemical shift frequency of individual molecules but have relatively poor concentration sensitivity. The poor concentration sensitivity of MR stems from low thermal nuclear spin polarization generated by typical MRI magnets, which align only about 1 in 100,000 nuclear spins. Accordingly traditional MR approaches require high concentrations of detected molecules.

To address the sensitivity challenge faced by MR approaches, hyperpolarization methods have been developed to align much larger fractions of nuclear spins and improve the sensitivity limits of NMR and MRI by several orders of magnitude.<sup>34-39</sup> Indeed, the first hyperpolarized (HP) contrast agent (<sup>129</sup>Xe gas)<sup>40-44</sup> has been FDA approved for ventilation lung imaging. Other HP molecular probes are also emerging for molecular imaging, including [1-<sup>13</sup>C]pyruvate.<sup>45</sup> HP [1-<sup>13</sup>C]pyruvate is similar to the [<sup>18</sup>F]fluorodeoxyglucose PET<sup>46,47</sup> tracer in that it allows molecular sensing of aberrant energy pathways in cancer<sup>35,36</sup> and many other diseases.<sup>48,49</sup> Currently in over 30 clinical trials, dissolution Dynamic Nuclear Polarization (d-DNP)<sup>50</sup> is the hyperpolarization method employed for production of HP [1-<sup>13</sup>C]pyruvate for molecular imaging applications. Hyperpolarized MRI has the ability to directly track and image metabolic events at any depth inside tissue at modest sub-mM concentrations and it is relatively safe because HP MRI uses injectable contrast agents that are endogenous biomolecules, instead of radioactive material. The disadvantages of d-DNP are that it is also highly infrastructure-intensive and relatively slow to build up hyperpolarization (~1 hour). A faster and simpler approach to hyperpolarize [1-<sup>13</sup>C]pyruvate is parahydrogen-induced polarization (PHIP).<sup>38,51-53</sup> One possibility is side-arm hydrogenation PHIP (SAH-PHIP),<sup>54,55</sup> which has been successfully used to hyperpolarize [1-

$^{13}\text{C}$ ]pyruvate,<sup>56–58</sup> the most common hyperpolarized MRI tracer. In SAH-PHIP an unsaturated side arm of a pyruvate ester is hydrogenated with parahydrogen, the polarization is transferred to the  $^{13}\text{C}$  nucleus, and the pyruvate is then cleaved via hydrolysis of the ester. Although SAH-PHIP is a successful approach for PHIP hyperpolarization of  $[1-^{13}\text{C}]$ pyruvate, the synthesis of the unsaturated pyruvate ester precursors is relatively complex and storage is not trivial. Unlike any existing method, Signal Amplification By Reversible Exchange (SABRE) hyperpolarizes sodium  $[1-^{13}\text{C}]$ pyruvate directly and without the need for chemical modifications.<sup>59,60</sup> As depicted in Fig. 1B, SABRE relies on reversible exchange of parahydrogen and a to-be-hyperpolarized substrate,  $[1-^{13}\text{C}]$ pyruvate, on an Ir-catalyst to create a spin network connecting parahydrogen and the target substrate. Continuous reversible exchange of parahydrogen and the substrate leads to rapid polarization build-up within the bulk  $[1-^{13}\text{C}]$ pyruvate molecules in solution. The resulting HP agent can be processed to quickly obtain biocompatibility for subsequent injection into the subject to monitor metabolic changes.

Since its inception,<sup>59–61</sup> SABRE hyperpolarization chemistry has undergone significant developments.<sup>62–65</sup> First, SABRE was primarily optimized to hyperpolarize protons in target substrates.<sup>59–61,66</sup> With the invention of the SABRE-SHEATH (SABRE in Shield Enables Alignment Transfer to Heteronuclei) variant, it became possible to efficiently hyperpolarize  $^{15}\text{N}$  and  $^{13}\text{C}$  nuclei that are associated with longer hyperpolarization lifetimes<sup>67–75</sup>—such as in  $[1-^{13}\text{C}]$ pyruvate.<sup>76,77</sup> Subsequent developments enabled polarization levels exceeding 10% using temperature cycling<sup>78,79</sup> and/or various pulsed-field approaches.<sup>80–83</sup> Building on these recent advances, here we show the first detection of a SABRE-hyperpolarized substrate,  $[1-^{13}\text{C}]$ pyruvate *in vivo*. Using a rat model, spectroscopic tracking of metabolic turnover and Chemical Shift Imaging (CSI) are demonstrated for kidney, liver, and whole body at multiple experimental sites,

pointing towards the development of a truly scalable molecular imaging technique resulting from the combination of fast, simple SABRE hyperpolarization chemistry with low-cost, cryogen-free MRI.<sup>84–88</sup>

## METHODS

### I. Sample Preparation

Under inert gas conditions,  $[1-^{13}\text{C}]$ pyruvate,  $[\text{Ir}(\text{IMes})(\text{COD})\text{Cl}]$  (IMes= 1,3 bis(2,4,6-trimethylphenyl)imidazole-2-ylidene, COD=cyclooctadiene) polarization-transfer pre-catalyst, and DMSO were mixed to give absolute concentrations of 65 mM  $[1-^{13}\text{C}]$ pyruvate, 24 mM DMSO, and 6 mM Ir-IMes in  $\text{CD}_3\text{OD}$ . Ir-IMes catalyst was synthesized using literature methods.<sup>89,90</sup> Dry  $\text{CD}_3\text{OD}$  was used as provided from the supplier (Cambridge Isotopes) and degassed with 5 freeze-pump-thaw cycles. All other chemicals used were purchased from Millipore Sigma.

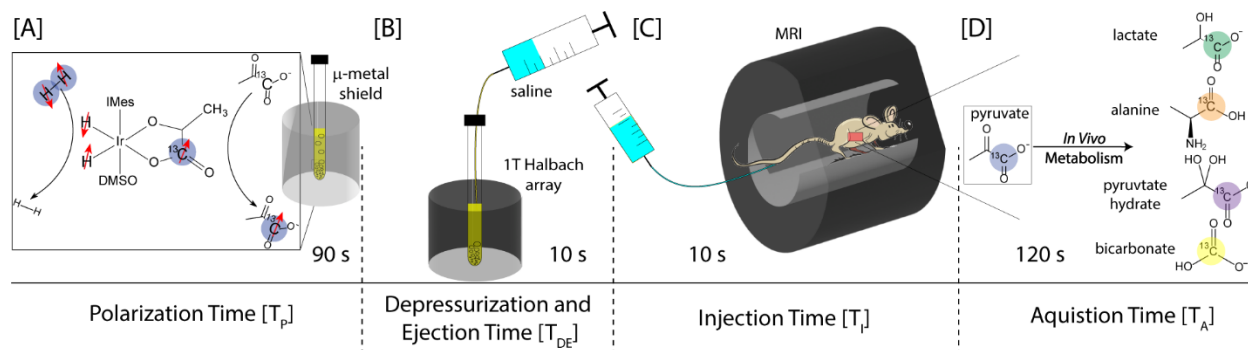


**Figure 2. Experimental procedure of MRI *in vivo* studies. [A] SABRE hyperpolarization takes place inside of a mu-magnetic shield at a polarization transfer field of  $0.3\ \mu\text{T}$ . The sample is pre-cooled to  $0^\circ\text{C}$  and then parahydrogen is bubbled through the solution for 90 seconds allowing for polarization buildup in the magnetic shields. [B] The sample is transferred to a 1 T Halbach array (to help slow relaxation of the hyperpolarization) for depressurization and ejection into a syringe pre-filled saline, taking 10 seconds. [C] After ejection the sample is moved across the room and attached to the catheter for injection, requiring  $\sim 10\ \text{s}$ . [D] After injection a two-minute scan is applied with a  $20^\circ$  pulse and repetition time of 2 seconds to detect the metabolic products of pyruvate—namely lactate, alanine, pyruvate-hydrate, and bicarbonate.**

## II. Hyperpolarization and sample processing

[1-<sup>13</sup>C]pyruvate was hyperpolarized by bubbling parahydrogen through a 500  $\mu$ L solution containing 6 mM Iridium-IMes catalyst, 24 mM DMSO, and 65 mM 1-<sup>13</sup>C Pyruvate at 100 psi inside a standard NMR tube using a previously described bubbling setup.<sup>79</sup> The sample is pre-cooled to 0 °C and then placed into a Polarization Transfer Field (PTF) of 0.3  $\mu$ T established in mu-metal shields provided by MagneticShield Corp. (ZG-203). After 90 s of bubbling parahydrogen, at room temperature and 0.3  $\mu$ T field, the sample is manually transferred into a 1 T Halbach array, where the parahydrogen pressure is released. The sample is subsequently pulled into a syringe prefilled with saline solution, creating a saline-methanol mixture. For the experiments at 4.7 T at Massachusetts General Hospital (MGH), 1.5 mL saline was used creating a total injectable volume of 2 mL, with a methanol-to-saline ratio of 1:3. These concentrations correspond to a dosage of 11.3 mg/kg (0.13 mmol/kg) of pyruvate injected into ~250 g Sprague Dawley rats. For the experiments at 1.5 T (at NC State) using the cryogen-free MRI system, only 1 mL of saline was used, creating a total injectable volume of 1.5 mL with a methanol-to-saline ratio of 1:2. These concentrations correspond to a dosage of 14.1 mg/kg (0.16 mmol/kg) of pyruvate injected into ~200 g Wistar rats. These dosages of hyperpolarized and injected pyruvate are lower than those in typical d-DNP hyperpolarized MRI studies, which are closer to (0.75 to 1 mmol/kg).<sup>91-95</sup> For all animal studies, the rats were sedated with isoflurane before placing them in the MRI scanner. Isoflurane was continuously provided via a nose cone in the MRI scanner during experimentation, and the heart and breathing rates were continuously monitored. The vitals remained stable after injection, and the animals were euthanized before waking from anesthesia approximately 10 minutes after completion of the experiment. All animal handling procedures were conducted under the appropriate IACUC protocols at NC State and MGH. At NC State,

hyperpolarized  $^{13}\text{C}$  MR data were acquired from the whole body of the animals. The cryogen-free, variable-field MRI system at NC State used whole body transmit/receive  $^{13}\text{C}$  volume coils (5.2 cm RF window length and 6.5 cm in diameter). At both sites, the spectroscopic data were obtained using a  $20^\circ$  non-selective 0.314 ms hard pulses, a repetition time (TR) of 2 seconds including a 0.68 s acquisition time, 12 kHz spectral bandwidth, and 8,192 spectral points.

At MGH, the hyperpolarized  $^{13}\text{C}$  animal experiment was conducted on a 4.7 T animal MRI scanner (Bruker Biospin, Billerica, USA) using a commercial transmit/receive proton volume coil (Bruker, Billerica, USA) for localization and shimming.  $^{13}\text{C}$  experiments used a custom-made transmit/receive  $^{13}\text{C}$  surface coil with a 6 cm inner diameter for  $^{13}\text{C}$  acquisitions. In the dynamic spectroscopy experiments, a pulse-and-acquire sequence was used with a non-selective 0.11 ms hard pulse, centered at 180 ppm with a  $30^\circ$  nominal flip angle and a repetition time (TR) of 3 s. For all chemical shift imaging (CSI) experiments, a sinc pulse with 11,000 Hz bandwidth and 0.56 ms length was used to selectively excite a single axial slice of 15 mm thickness. CSI parameters were, TR 410 ms, echo time (TE) 1.05 ms,  $20^\circ$  nominal flip angle, spectral bandwidth 10,080 Hz, 4,096 spectral points, field of view (FOV) of 80 mm  $\times$  40 mm, and matrix size 8  $\times$  8.

## RESULTS AND DISCUSSION

### *I. In Vivo Spectroscopy at 4.7 T*

Figure 3 shows the data obtained for the first observation of metabolic conversion using dynamic spectroscopy employing SABRE-hyperpolarized  $[1-^{13}\text{C}]$ pyruvate. The surface coil was placed either on the liver or the kidney of the rat, the hyperpolarization was started, followed by dilution with saline, injection, and data acquisition. As seen in Fig. 3, the data clearly show peaks for lactate, alanine, pyruvate-hydrate, and bicarbonate. Figures 3A-C show the data acquired from the liver, and Figures 3D-F from the kidney. In comparison, the data from the liver clearly shows a

higher metabolic rate as expected,<sup>91</sup> while noting that in the presented pilot studies significant quantities of methanol were injected, which is known to alter metabolism.<sup>96,97</sup> Future work will use ethanol/water or fully aqueous injectables.<sup>98</sup> Figs. 3A and D show spectra created by summing the data across the full time duration for liver and kidney, respectively. Most metabolic turnover is observed to lactate and alanine, whereas conversion to pyruvate-hydrate and bicarbonate is less pronounced. Figs. 3B and E show the full time-resolved spectra. Figs. 3C and F show the corresponding projection of the signals for pyruvate, lactate, and alanine as a function of time, revealing the time course of pyruvate perfusion convoluted with metabolic conversion and  $T_1$  relaxation for the individual metabolites—as expected from previous d-DNP work.<sup>91</sup> As can be seen, metabolic tracking for about one minute was possible in these first proof-of-concept studies.

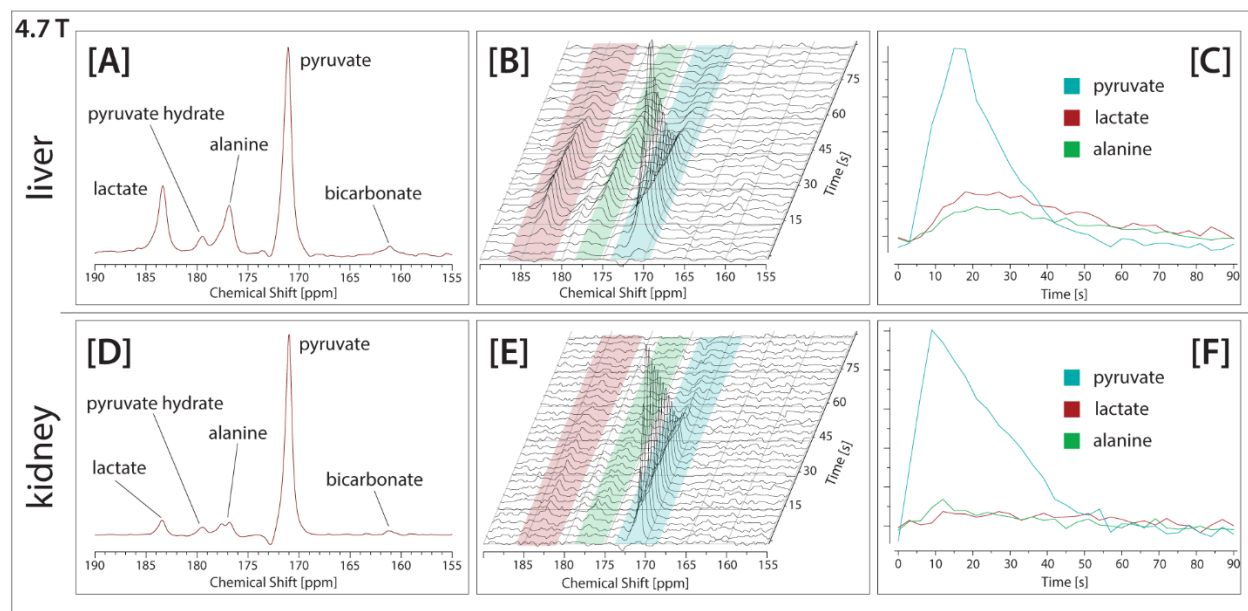


**Figure 3.** *In vivo* spectra acquired on two (Sprague Dawley, female) rats using a dynamic spectroscopy sequence and a different field of view on the liver [A-C] and kidney [D-F]. [A, D] Summed spectra of the complete dynamic spectroscopy acquisition. [B, E] Spectra overlay of the dynamic spectroscopy acquisition with lactate (red), alanine (green), and pyruvate (blue) integration regions highlighted. [C, F] Plot of the integrated acquisition for pyruvate, lactate, and alanine using the spectra shown in B and E. The spectra in this temporal series are acquired with 30° flip angle and 3 s delay between acquisitions.

## II. *In Vivo* Spectroscopic Imaging at 4.7 T

In addition to *in vivo* spectroscopy, we implemented Chemical Shift Imaging (CSI) to visualize the spatial distribution of the SABRE-hyperpolarized  $[1-^{13}\text{C}]$ pyruvate within the kidney and liver as displayed in Fig. 4. The individual spectra were integrated and turned into a heat map superimposed on an anatomical proton-MRI slice of the imaged region. Figs. 4A-C show the data acquired with the surface coil placed on the liver, whereas Figs. 4D-E show the data acquired when the surface coil was placed on the kidney. Figs. 4A and D show the respective raw CSI data displaying the spectra acquired in a  $8 \times 8$  grid covering a field of view (FOV) of  $8 \times 4$  cm. Figs. 4B and E each show a heatmap over the corresponding anatomical image, which was then smoothed by zero-filling the data to assist with visualization—as shown in Figs. 4C and F. In this work, the excitation pulses were selectively applied on the  $1-^{13}\text{C}$  pyruvate peaks to ensure visibility and sufficient signal-to-noise. The liver image shows most pyruvate signal primarily centered around the hepatic vein, whereas the kidney image shows most pyruvate signal centered around the renal vein. To additionally visualize the metabolic products, pulse program modifications would be necessary that are beyond the scope of this current first demonstration. Accordingly, the current imaging data does not contain information on the metabolic products and only visualized the SABRE-hyperpolarized  $[1-^{13}\text{C}]$ pyruvate; nevertheless, the CSI approach will be critical in future studies imaging disease models, where the production of metabolites may be strongly modulated. For example, the production of lactate is often greatly increased in the presence of tumors because of the Warburg effect.<sup>36,99–103</sup>

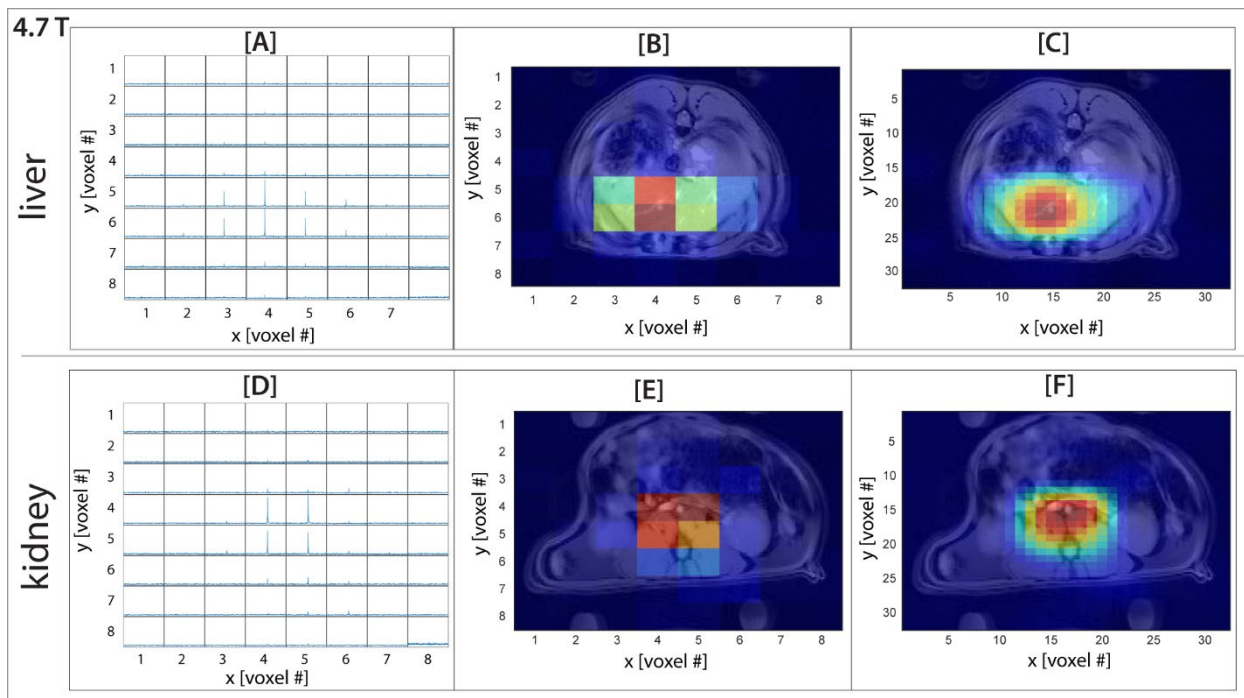


**Figure 4. Chemical Shift Imaging (CSI) experiments performed on two separate animals (shown in separate rows) with two different fields of view (liver, row 1; kidney, row 2). [A, D] 8×8 array of the 64 spectra acquired in the respective CSI experiments. [B, E] Integration of the peaks shown in the spectra to obtain a heat map overlaid on top of the center anatomical slice of the imaged region. [C, F] Linearly extrapolated heat map (32×32) for visualization of the CSI results. CSI results are acquired linearly in a 8×8 matrix using a 20° flip angle and a 0.41 s TR.**

### III. Cryogen-Free 1.5 T Hyperpolarized *In Vivo* Spectroscopy

In tandem with the work performed at MGH, experiments were conducted at NC State using a cryogen-free variable-field MRI scanner. The use of a cryogen-free MRI and lower magnetic fields circumvents the need for large amounts of helium, reducing installation and maintenance costs. Even the combination with portable bedside (“point-of-care”) MRI<sup>84,85</sup> becomes imaginable. The variable field of our unique MRI (5 mT – 3 T) assists with the broader translation into clinical settings, as the common clinical fields are between 1.5 – 3 T. Studies closely comparable to those performed on the preclinical 4.7 T MGH scanner are shown here. Differences reside in the use of

a whole body volume coil instead of surface coils, slightly smaller animals (~200 g versus ~250 g), and operation at 1.5 T. The selection of 1.5 T helps to establish direct correlation to more clinical settings often operating at this field. Figure 5A shows summed spectra of the hyperpolarized pyruvate, along with its downstream metabolic products lactate and alanine, as well as the other (minor) byproducts—pyruvate-hydrate and bicarbonate. Since the 1.5 T data is acquired using a full-body coil, the signal represents an average across the whole rat, showing lower metabolic activity in comparison to the [1-<sup>13</sup>C]pyruvate signal from the liver and kidney (which are more metabolically active organs). In addition, shimming the magnetic field over a full body is more challenging than over individual organs, which is reflected in broader spectral features visible in Figure 5 A, in contrast to those from Figures 3A and C. Despite these challenges hyperpolarized signal is detectable for over one minute, and time-resolved metabolism could be observed as illustrated in Figs. 5B and C—presented in analogy to Fig. 3. Overall, the experiments shown in Figure 5 indicate the successful combination of low-cost hyperpolarization with low-cost MRI to achieve *in vivo* detection of metabolic transformations, advancing this technology and setting the stage for future developments and biomedical applications.

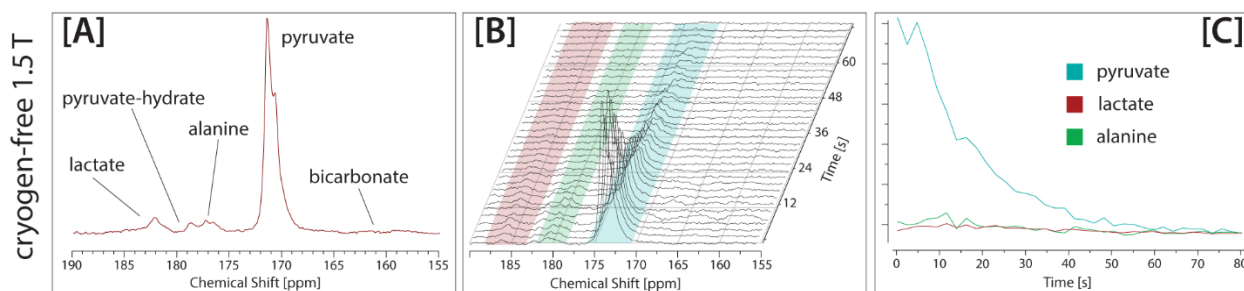


**Figure 5.** *In vivo* spectra acquired on one [Wistar, female] rat using a dynamic spectroscopy sequence. [A] Summed spectra of the complete dynamic spectroscopy acquisition. [B] Spectra overlay of the dynamic spectroscopy acquisition with lactate (red), alanine (green), and pyruvate (blue) integration regions highlighted. [C] Plot of the integrated acquisition for pyruvate, lactate, and alanine using the spectra shown in B. The spectra in this temporal series are acquired with a 20-degree flip angle and a 2 s delay between acquisitions.

## CONCLUSION

The first *in vivo* metabolic hyperpolarized MRI experiments were demonstrated using SABRE hyperpolarization chemistry and  $[1-^{13}\text{C}]$ pyruvate as an exogenous molecular probe.  $[1-^{13}\text{C}]$ pyruvate is the leading molecular probe because it is a key metabolite that is often dysregulated in many disease states. *In vivo* studies were performed on two different instruments at two different sites to provide multi-site validation of the emerging SABRE technology: a 4.7 T magnet at MGH and a 1.5 T cryogen-free magnet at NC State. Both systems showed good signal-to-noise for the detection of SABRE-hyperpolarized  $[1-^{13}\text{C}]$ pyruvate and enabled real-time metabolic tracking of the formation of lactate, alanine, pyruvate-hydrate, and bicarbonate. The presented work is a key milestone in the translation of SABRE hyperpolarization chemistry—which has been under development for almost 15 years since inception—to pre-clinical applications focused on biomedical questions. Future work still has to address challenges associated with full biocompatibility given that in the presented work significant methanol fractions were in the solutions as well as Iridium based polarization transfer catalyst. Ongoing work shows clear pathways towards catalyst-free ethanol/water or fully aqueous formulations,<sup>98</sup> which will be used in forthcoming work. Notwithstanding, the facile nature of SABRE hyperpolarization chemistry makes SABRE based technology a good candidate for broader dissemination with the potential to become competitive in the landscape of existing molecular imaging technologies, and medical imaging at large. Specifically, the combination of portable, low-field MRI approaches that otherwise suffer from significant sensitivity limitations could be combined with SABRE hyperpolarization chemistry to deliver broadly available molecular imaging with the ability to track individual metabolic pathways.

## ACKNOWLEDGMENTS

This work was supported by the NSF under grants CHE-1904780 and CHE-1905341, and the National Institutes of Health (NIH) under R01EB029829, S10OD021768, and R21GM137227. The content is solely the responsibility of the authors and does not necessarily represent the official views of the NIH. TT also acknowledges funding from the Goodnight foundation. MSR acknowledges the gracious support of the Kiyomi and Ed Baird MGH Research Scholar Award.

## AUTHOR INFORMATION

### Corresponding Authors

\* Patrick TomHon: [patrick@vizmalifesciences.com](mailto:patrick@vizmalifesciences.com)

\* Thomas Theis: [ttheis@ncsu.edu](mailto:ttheis@ncsu.edu)

### Conflict of Interest Disclosures

PT, CD, TT and MSR are co-founders and equity holders of Vizma Life Sciences (VLS). CD and PT are employees of VLS. EYC is an equity holder of Vizma Life Sciences. The terms of TT's arrangement have been reviewed and approved by NC State University in accordance with its policy on objectivity in research. EYC and BMG hold ownership stakes in XeUS Technologies Ltd. MSR is a founder and equity holder of Hyperfine Inc. All other authors declare that they have no competing interest.

## REFERENCES

- (1) Prichard, J. W.; Brass, L. M. New Anatomical and Functional Imaging Methods. *Ann Neurol* **1992**, *32* (3), 395–400. <https://doi.org/https://doi.org/10.1002/ana.410320316>.
- (2) Histed, S. N.; Lindenberg, M. L.; Mena, E.; Turkbey, B.; Choyke, P. L.; Kurdziel, K. A. Review of Functional/Anatomical Imaging in Oncology. *Nucl Med Commun* **2012**, *33* (4). <https://doi.org/10.1097/MNM.0b013e32834ec8a5>.
- (3) Pysz, M. A.; Gambhir, S. S.; Willmann, J. K. Molecular Imaging: Current Status and Emerging Strategies. *Clin Radiol* **2010**, *65* (7), 500–516. <https://doi.org/10.1016/J.CRAD.2010.03.011>.
- (4) Weissleder, R.; Mahmood, U. Molecular Imaging. *Radiology* **2001**, *219* (2), 316–333. <https://doi.org/10.1148/radiology.219.2.r01ma19316>.
- (5) Kircher, M. F.; Willmann, J. K. Molecular Body Imaging: MR Imaging, CT, and US. Part I. Principles. *Radiology* **2012**, *263* (3), 633–643. <https://doi.org/10.1148/radiol.12102394>.
- (6) Lauterbur, P. C. Image Formation by Induced Local Interactions: Examples Employing Nuclear Magnetic Resonance. *Nature* **1973**, *242* (5394), 190–191.
- (7) Grover, V. P. B.; Tognarelli, J. M.; Crossey, M. M. E.; Cox, I. J.; Taylor-Robinson, S. D.; McPhail, M. J. W. Magnetic Resonance Imaging: Principles and Techniques: Lessons for Clinicians. *J Clin Exp Hepatol* **2015**, *5* (3), 246. <https://doi.org/10.1016/J.JCEH.2015.08.001>.
- (8) Wells, P. N. T. Ultrasound Imaging. *Phys Med Biol* **2006**, *51* (13), R83. <https://doi.org/10.1088/0031-9155/51/13/R06>.

- (9) Aldrich, J. E. Basic Physics of Ultrasound Imaging. *Crit Care Med* **2007**, *35* (5 SUPPL.). <https://doi.org/10.1097/01.CCM.0000260624.99430.22>.
- (10) Haddad, W. S.; McNulty, I.; Trebes, J. E.; Anderson, E. H.; Levesque, R. A.; Yang, L. Ultrahigh-Resolution x-Ray Tomography. *Science (1979)* **1994**, *266* (5188), 1213–1215. <https://doi.org/10.1126/SCIENCE.266.5188.1213>.
- (11) Seibert, J. A.; Boone, J. M. X-Ray Imaging Physics for Nuclear Medicine Technologists. Part 2: X-Ray Interactions and Image Formation. *J Nucl Med Technol* **2005**, *33* (1).
- (12) Seibert, J. A. X-Ray Imaging Physics for Nuclear Medicine Technologists. Part 1: Basic Principles of X-Ray Production. *J Nucl Med Technol* **2004**, *32* (3).
- (13) Pelc, N. J. Recent and Future Directions in CT Imaging. *Ann Biomed Eng* **2014**, *42* (2), 260–268. <https://doi.org/10.1007/s10439-014-0974-z>.
- (14) Hallouard, F.; Anton, N.; Choquet, P.; Constantinesco, A.; Vandamme, T. Iodinated Blood Pool Contrast Media for Preclinical X-Ray Imaging Applications – A Review. *Biomaterials* **2010**, *31* (24), 6249–6268. <https://doi.org/10.1016/j.biomaterials.2010.04.066>.
- (15) Tootell, R. B.; Reppas, J. B.; Kwong, K. K.; Malach, R.; Born, R. T.; Brady, T. J.; Rosen, B. R.; Belliveau, J. W. Functional Analysis of Human MT and Related Visual Cortical Areas Using Magnetic Resonance Imaging. *The Journal of Neuroscience* **1995**, *15* (4), 3215. <https://doi.org/10.1523/JNEUROSCI.15-04-03215.1995>.
- (16) Cohen, M. S.; Kosslyn, S. M.; Breiter, H. C.; DiGirolamo, G. J.; Thompson, W. L.; Anderson, A. K.; Bookheimer, S. Y.; Rosen, B. R.; Belliveau, J. W. Changes in Cortical Activity during Mental Rotation A Mapping Study Using Functional MRI. *Brain* **1996**, *119* (1), 89–100. <https://doi.org/10.1093/brain/119.1.89>.
- (17) Logothetis, N. K. What We Can Do and What We Cannot Do with fMRI. *Nature* **2008**, *453* (7197), 869–878. <https://doi.org/10.1038/nature06976>.
- (18) Rosen, B. R.; Savoy, R. L. fMRI at 20: Has It Changed the World? *Neuroimage* **2012**, *62* (2), 1316–1324. <https://doi.org/10.1016/J.NEUROIMAGE.2012.03.004>.
- (19) Grade, M.; Hernandez Tamames, J. A.; Pizzini, F. B.; Achten, E.; Golay, X.; Smits, M. A. Neuroradiologist’s Guide to Arterial Spin Labeling MRI in Clinical Practice. *Neuroradiology* **2015**, *57* (12), 1181–1202. <https://doi.org/10.1007/s00234-015-1571-z>.
- (20) Golay, X.; Hendrikse, J.; Lim, T. C. C. Perfusion Imaging Using Arterial Spin Labeling. *Topics in Magnetic Resonance Imaging* **2004**, *15* (1). <https://doi.org/10.1097/00002142-200402000-00003>.
- (21) Detre, J. A.; Wang, J.; Wang, Z.; Rao, H. Arterial Spin-Labeled Perfusion MRI in Basic and Clinical Neuroscience. *Curr Opin Neurol* **2009**, *22* (4). <https://doi.org/10.1097/WCO.0b013e32832d9505>.
- (22) Le Bihan, D.; Mangin, J. F.; Poupon, C.; Clark, C. A.; Pappata, S.; Molko, N.; Chabriat, H. Diffusion Tensor Imaging: Concepts and Applications. *Journal of Magnetic Resonance Imaging* **2001**, *13* (4), 534–546. <https://doi.org/10.1002/JMRI.1076>.
- (23) Alexander, A. L.; Lee, J. E.; Lazar, M.; Field, A. S. Diffusion Tensor Imaging of the Brain. *Neurotherapeutics* **2007**, *4* (3), 316–329. <https://doi.org/10.1016/J.NURT.2007.05.011>.

- (24) Rubin, G. D.; Leipsic, J.; Joseph Schoepf, U.; Fleischmann, D.; Napel, S. CT Angiography after 20 Years: A Transformation in Cardiovascular Disease Characterization Continues to Advance. *Radiology* **2014**, *271* (3), 633–652. <https://doi.org/10.1148/RADIOL.14132232>.
- (25) Fang, C.; Sidhu, P. S. Ultrasound-Based Liver Elastography: Current Results and Future Perspectives. *Abdominal Radiology* *2020 45:11* **2020**, *45* (11), 3463–3472. <https://doi.org/10.1007/S00261-020-02717-X>.
- (26) Kubota, K. From Tumor Biology to Clinical PET: A Review of Positron Emission Tomography (PET) in Oncology. *Ann Nucl Med* **2001**, *15* (6), 471–486. <https://doi.org/10.1007/BF02988499>.
- (27) Vaquero, J. J.; Kinahan, P. Positron Emission Tomography: Current Challenges and Opportunities for Technological Advances in Clinical and Preclinical Imaging Systems. *Annu Rev Biomed Eng* **2015**, *17*, 385–414. <https://doi.org/10.1146/ANNUREV-BIOENG-071114-040723>.
- (28) Hangel, G.; Niess, E.; Lazen, P.; Bednarik, P.; Bogner, W.; Strasser, B. Emerging Methods and Applications of Ultra-High Field MR Spectroscopic Imaging in the Human Brain. *Anal Biochem* **2022**, *638*, 114479. <https://doi.org/10.1016/J.AB.2021.114479>.
- (29) Kurhanewicz, J.; Vigneron, D. B.; Nelson, S. J. Three-Dimensional Magnetic Resonance Spectroscopic Imaging of Brain and Prostate Cancer. *Neoplasia* **2000**, *2* (1–2), 166–189. <https://doi.org/10.1038/SJ.NEO.7900081>.
- (30) Maudsley, A. A.; Domenig, C.; Govind, V.; Darkazanli, A.; Studholme, C.; Arheart, K.; Bloomer, C. Mapping of Brain Metabolite Distributions by Volumetric Proton MR Spectroscopic Imaging (MRSI). *Magn Reson Med* **2009**, *61* (3), 548–559. <https://doi.org/10.1002/MRM.21875>.
- (31) van Zijl, P. C. M.; Brindle, K.; Lu, H.; Barker, P. B.; Edden, R.; Yadav, N.; Knutsson, L. Hyperpolarized MRI, Functional MRI, MR Spectroscopy and CEST to Provide Metabolic Information in Vivo. *Curr Opin Chem Biol* **2021**, *63*, 209–218. <https://doi.org/10.1016/J.CBPA.2021.06.003>.
- (32) Goldenberg, J. M.; Pagel, M. D. Assessments of Tumor Metabolism with CEST MRI. *NMR Biomed* **2019**, *32* (10), e3943. <https://doi.org/10.1002/NBM.3943>.
- (33) Jones, K. M.; Pollard, A. C.; Pagel, M. D.; Pagel, M.; Jones, K.; Pollard, A. Clinical Applications of Chemical Exchange Saturation Transfer (CEST) MRI. *J Magn Reson Imag* **2018**, *47* (1), 11–27. <https://doi.org/10.1002/JMRI.25838>.
- (34) Eills, J.; Budker, D.; Cavagnero, S.; Chekmenev, E. Y.; Elliott, S. J.; Jannin, S.; Lesage, A.; Matysik, J.; Meersmann, T.; Prisner, T.; Reimer, J. A.; Yang, H.; Koptuyg, I. V. Spin Hyperpolarization in Modern Magnetic Resonance. *Chem Rev* **2023**. <https://doi.org/doi.org/10.1021/acs.chemrev.2c00534>.
- (35) Nelson, S. J.; Kurhanewicz, J.; Vigneron, D. B.; Larson, P. E. Z.; Harzstark, A. L.; Ferrone, M.; Van Criekinge, M.; Chang, J. W.; Bok, R.; Park, I.; Reed, G.; Carvajal, L.; Small, E. J.; Munster, P.; Weinberg, V. K.; Ardenkjaer-Larsen, J. H.; Chen, A. P.; Hurd, R. E.; Odegardstuen, L. I.; Robb, F. J.; Tropp, J.; Murray, J. A. Metabolic Imaging of Patients with Prostate Cancer Using Hyperpolarized [1-13C]Pyruvate. *Sci Transl Med* **2013**, *5* (198). <https://doi.org/10.1126/scitranslmed.3006070>.

- (36) Kurhanewicz, J.; Vigneron, D. B.; Ardenkjaer-Larsen, J. H.; Bankson, J. A.; Brindle, K.; Cunningham, C. H.; Gallagher, F. A.; Keshari, K. R.; Kjaer, A.; Laustsen, C.; Mankoff, D. A.; Merritt, M. E.; Nelson, S. J.; Pauly, J. M.; Lee, P.; Ronen, S.; Tyler, D. J.; Rajan, S. S.; Spielman, D. M.; Wald, L.; Zhang, X.; Malloy, C. R.; Rizi, R. Hyperpolarized  $^{13}\text{C}$  MRI: Path to Clinical Translation in Oncology. *Neoplasia* **2019**, *21* (1), 1–16. <https://doi.org/10.1016/J.NEO.2018.09.006>.
- (37) Wang, Z. J.; Ohliger, M. A.; Larson, P. E. Z.; Gordon, J. W.; Bok, R. A.; Slater, J.; Villanueva-Meyer, J. E.; Hess, C. P.; Kurhanewicz, J.; Vigneron, D. B. Hyperpolarized  $^{13}\text{C}$  MRI: State of the Art and Future Directions. *Radiology* **2019**, *291* (2), 273–284. <https://doi.org/doi.org/10.1148/radiol.2019182391>.
- (38) Hövener, J. B.; Pravdivtsev, A. N.; Kidd, B.; Bowers, C. R.; Glöggler, S.; Kovtunov, K. V.; Plaumann, M.; Katz-Brull, R.; Buckenmaier, K.; Jerschow, A.; Reineri, F.; Theis, T.; Shchepin, R. V.; Wagner, S.; Bhattacharya, P.; Zacharias, N. M.; Chekmenev, E. Y. Parahydrogen-Based Hyperpolarization for Biomedicine. *Angew Chem Int Ed* **2018**, *57* (35), 11140–11162. <https://doi.org/10.1002/ANIE.201711842>.
- (39) Kovtunov, K. V.; Pokochueva, E. V.; Salnikov, O. G.; Cousin, S. F.; Kurzbach, D.; Vuichoud, B.; Jannin, S.; Chekmenev, E. Y.; Goodson, B. M.; Barskiy, D. A.; Koptuyug, I. V. Hyperpolarized NMR Spectroscopy: D-DNP, PHIP, and SABRE Techniques. *Chem Asian J* **2018**, *13* (15), 1857–1871. <https://doi.org/10.1002/ASIA.201800551>.
- (40) Walkup, L. L.; Woods, J. C. Translational Applications of Hyperpolarized  $^3\text{He}$  and  $^{129}\text{Xe}$ . *NMR Biomed* **2014**, *27* (12), 1429–1438. <https://doi.org/10.1002/NBM.3151>.
- (41) Mugler, J. P.; Altes, T. A. Hyperpolarized  $^{129}\text{Xe}$  MRI of the Human Lung. *Journal of Magnetic Resonance Imaging* **2013**, *37* (2), 313–331. <https://doi.org/10.1002/JMRI.23844>.
- (42) Grist, J. T.; Collier, G. J.; Walters, H.; Kim, M.; Chen, M.; Abu Eid, G.; Laws, A.; Matthews, V.; Jacob, K.; Cross, S.; Eves, A.; Durrant, M.; McIntyre, A.; Thompson, R.; Schulte, R. F.; Raman, B.; Robbins, P. A.; Wild, J. M.; Fraser, E.; Gleeson, F. Lung Abnormalities Detected with Hyperpolarized  $^{129}\text{Xe}$  MRI in Patients with Long COVID. *Radiology* **2022**, *305* (3), 709–717. <https://doi.org/doi.org/10.1148/radiol.220069>.
- (43) Barskiy, D. A.; Coffey, A. M.; Nikolaou, P.; Mikhaylov, D. M.; Goodson, B. M.; Branca, R. T.; Lu, G. J.; Shapiro, M. G.; Telkki, V. V.; Zhivonitko, V. V.; Koptuyug, I. V.; Salnikov, O. G.; Kovtunov, K. V.; Bukhtiyarov, V. I.; Rosen, M. S.; Barlow, M. J.; Safavi, S.; Hall, I. P.; Schröder, L.; Chekmenev, E. Y. NMR Hyperpolarization Techniques of Gases. *Chemistry – A European Journal* **2017**, *23* (4), 725–751. <https://doi.org/10.1002/CHEM.201603884>.
- (44) Nikolaou, P.; Goodson, Boyd, M.; Chekmenev, E. Y. NMR Hyperpolarization Techniques for Biomedicine. *Chem. Eur. J.* **2015**, *21* (8), 3156–3166. <https://doi.org/10.1002/chem.201405253>.
- (45) Brindle, K. M.; Keshari, K. R. Editorial Commentary for the Special Issue: Technological Developments in Hyperpolarized  $^{13}\text{C}$  Imaging—toward a Deeper Understanding of Tumor Metabolism in Vivo. *Magnetic Resonance Materials in Physics, Biology and Medicine* **2021**, *34* (1), 1–3. <https://doi.org/10.1007/s10334-021-00908-1>.
- (46) Fletcher, J. W.; Djulbegovic, B.; Soares, H. P.; Siegel, B. A.; Lowe, V. J.; Lyman, G. H.; Coleman, R. E.; Wahl, R.; Paschold, J. C.; Avril, N.; Einhorn, L. H.; Suh, W. W.; Samson, D.;

- Delbeke, D.; Gorman, M.; Shields, A. F. Recommendations on the Use of 18F-FDG PET in Oncology. *Journal of Nuclear Medicine* **2008**, *49* (3), 480–508. <https://doi.org/10.2967/JNUMED.107.047787>.
- (47) Basu, S.; Hess, S.; Nielsen Braad, P. E.; Olsen, B. B.; Inglev, S.; Høiland-Carlsen, P. F. The Basic Principles of FDG-PET/CT Imaging. *PET Clin* **2014**, *9* (4), 355–370. <https://doi.org/10.1016/J.CPET.2014.07.006>.
- (48) Cunningham, C. H.; Lau, J. Y. C.; Chen, A. P.; Geraghty, B. J.; Perks, W. J.; Roifman, I.; Wright, G. A.; Connelly, K. A. Hyperpolarized <sup>13</sup>C Metabolic MRI of the Human Heart: Initial Experience. *Circ Res* **2016**, *119* (11). <https://doi.org/10.1161/CIRCRESAHA.116.309769>.
- (49) Rider, O. J.; Apps, A.; Miller, J. J. J.; Lau, J. Y. C.; Lewis, A. J. M.; Peterzan, M. A.; Dodd, M. S.; Lau, A. Z.; Trumper, C.; Gallagher, F. A.; Grist, J. T.; Brindle, K. M.; Neubauer, S.; Tyler, D. J. Noninvasive In Vivo Assessment of Cardiac Metabolism in the Healthy and Diabetic Human Heart Using Hyperpolarized <sup>13</sup>C MRI. *Circ Res* **2020**, 725–736. <https://doi.org/10.1161/CIRCRESAHA.119.316260>.
- (50) Ardenkjær-Larsen, J. H.; Fridlund, B.; Gram, A.; Hansson, G.; Hansson, L.; Lerche, M. H.; Servin, R.; Thaning, M.; Golman, K. Increase in Signal-to-Noise Ratio of >10,000 Times in Liquid-State NMR. *Proc Natl Acad Sci U S A* **2003**, *100* (18), 10158–10163. <https://doi.org/10.1073/pnas.1733835100>.
- (51) Bowers, C. R.; Weitekamp, D. P. Parahydrogen and Synthesis Allow Dramatically Enhanced Nuclear Alignment. *J Am Chem Soc* **1987**, *109* (18), 5541–5542. <https://doi.org/10.1021/ja00252a049>.
- (52) Bowers, C. R.; Weitekamp, D. P. Transformation of Symmetrization Order to Nuclear-Spin Magnetization by Chemical-Reaction and Nuclear-Magnetic-Resonance. *Phys. Rev. Lett.* **1986**, *57* (21), 2645–2648. <https://doi.org/10.1103/PhysRevLett.57.2645>.
- (53) Schmidt, A.; Bowers, C.; Buckenmeier, K.; Chekmenev, E.; de Maissin, H.; Eills, J.; Ellermann, F.; Gloggler, S.; Gordon, J.; Knecht, S.; Koptuyug, I.; Kuhn, J.; Pravdivtsev, A.; Reineri, F.; Theis, T.; Them, K.; Hövener, J.-B. Instrumentation for Hydrogenative Parahydrogen-Based Hyperpolarization Techniques. *Anal Chem* *94* (1), 479–502. <https://doi.org/10.1021/acs.analchem.1c04863>.
- (54) Reineri, F.; Boi, T.; Aime, S. ParaHydrogen Induced Polarization of <sup>13</sup>C Carboxylate Resonance in Acetate and Pyruvate. *Nat Commun* **2015**, *6* (1), 1–6. <https://doi.org/10.1038/ncomms6858>.
- (55) Cavallari, E.; Carrera, C.; Aime, S.; Reineri, F. Studies to Enhance the Hyperpolarization Level in PHIP-SAH-Produced <sup>13</sup>C-Pyruvate. *Journal of Magnetic Resonance* **2018**, *289*, 12–17. <https://doi.org/10.1016/j.jmr.2018.01.019>.
- (56) Svyatova, A.; Kozinenko, V. P.; Chukanov, N. V.; Burueva, D. B.; Chekmenev, E. Y.; Chen, Y. W.; Hwang, D. W.; Kovtunov, K. V.; Koptuyug, I. V. PHIP Hyperpolarized [1-<sup>13</sup>C]Pyruvate and [1-<sup>13</sup>C]Acetate Esters via PH-INEPT Polarization Transfer Monitored by <sup>13</sup>C NMR and MRI. *Sci Rep* **2021**, *11* (1), 5646. <https://doi.org/10.1038/S41598-021-85136-2>.
- (57) Hune, T.; Mamone, S.; Schroeder, H.; Jagtap, A. P.; Sternkopf, S.; Stevanato, G.; Korchak, S.; Fokken, C.; Müller, C. A.; Schmidt, A. B.; Becker, D.; Glögger, S. Metabolic Tumor Imaging

- with Rapidly Signal-Enhanced 1-<sup>13</sup>C-Pyruvate-D<sub>3</sub>. *ChemPhysChem* **2023**, *24* (2), e202200615. <https://doi.org/10.1002/CPHC.202200615>.
- (58) Stevanato, G.; Ding, Y.; Mamone, S.; Jagtap, A. P.; Korchak, S.; Glöggler, S. Real-Time Pyruvate Chemical Conversion Monitoring Enabled by PHIP. *J Am Chem Soc* **2022**, *145*, 15. <https://doi.org/doi.org/10.1021/jacs.2c13198>.
- (59) Adams, R. W.; Aguilar, J. A.; Atkinson, K. D.; Cowley, M. J.; Elliott, P. I. P.; Duckett, S. B.; Green, G. G. R.; Khazal, I. G.; Lopez-Serrano, J.; Williamson, D. C. Reversible Interactions with Para-Hydrogen Enhance NMR Sensitivity by Polarization Transfer. *Science (1979)* **2009**, *323* (5922), 1708–1711. <https://doi.org/10.1126/science.1168877>.
- (60) Atkinson, K. D.; Cowley, M. J.; Duckett, S. B.; Elliott, P. I. P.; Green, G. G. R.; López-Serrano, J.; Khazal, I. G.; Whitwood, A. C. Para-Hydrogen Induced Polarization without Incorporation of Para-Hydrogen into the Analyte. *Inorg Chem* **2009**, *48* (2), 663–670. <https://doi.org/10.1021/ic8020029>.
- (61) Atkinson, K. D.; Cowley, M. J.; Elliott, P. I. P.; Duckett, S. B.; Green, G. G. R.; López-Serrano, J.; Whitwood, A. C. Spontaneous Transfer of Parahydrogen Derived Spin Order to Pyridine at Low Magnetic Field. *J Am Chem Soc* **2009**, *131* (37), 13362–13368. <https://doi.org/10.1021/ja903601p>.
- (62) Rayner, P. J.; Duckett, S. B. Signal Amplification by Reversible Exchange (SABRE): From Discovery to Diagnosis. *Angew. Chem. Int. Ed.* **2018**, *57* (23), 6742–6753. <https://doi.org/10.1002/anie.201710406>.
- (63) Roy, S. S.; Appleby, K. M.; Fear, E. J.; Duckett, S. B. SABRE-Relay: A Versatile Route to Hyperpolarization. *Journal of Physical Chemistry Letters* **2018**, *9* (5), 1112–1117. <https://doi.org/10.1021/acs.jpcclett.7b03026>.
- (64) Iali, W.; Rayner, P. J.; Duckett, S. B. Using Parahydrogen to Hyperpolarize Amines, Amides, Carboxylic Acids, Alcohols, Phosphates, and Carbonates. *Sci Adv* **2018**, *4* (1). <https://doi.org/10.1126/sciadv.aao6250>.
- (65) Olaru, A. M.; Burns, M. J.; Green, G. G. R.; Duckett, S. B. SABRE Hyperpolarisation of Vitamin B<sub>3</sub> as a Function of PH. *Chem Sci* **2017**, *8* (3), 2257–2266. <https://doi.org/10.1039/c6sc04043h>.
- (66) Roy, S. S.; Norcott, P.; Rayner, P. J.; Green, G. G. R.; Duckett, S. B. A Hyperpolarizable <sup>1</sup>H Magnetic Resonance Probe for Signal Detection 15 Minutes after Spin Polarization Storage. *Angewandte Chemie* **2016**, *128* (50), 15871–15874. <https://doi.org/10.1002/ange.201609186>.
- (67) Truong, M.; Theis, T.; Coffey, A.; Shchepin, R.; Waddell, K.; Shi, F.; Goodson, B.; Warren, W.; Chekmenev, E. 15N Hyperpolarization by Reversible Exchange Using SABRE-SHEATH. *The Journal of Physical Chemistry C* **2015**, *119* (16), 8786–8797. <https://doi.org/10.1021/acs.jpcc.5b01799>.
- (68) Shchepin, R. V.; Barskiy, D. A.; Coffey, A. M.; Theis, T.; Shi, F.; Warren, W. S.; Goodson, B. M.; Chekmenev, E. Y. 15N Hyperpolarization of Imidazole-15N<sub>2</sub> for Magnetic Resonance PH Sensing via SABRE-SHEATH. *ACS Sens* **2016**, *1* (6), 640–644. <https://doi.org/10.1021/acssensors.6b00231>.

- (69) Theis, T.; Truong, M. L.; Coffey, A. M.; Shchepin, R. V.; Waddell, K. W.; Shi, F.; Goodson, B. M.; Warren, W. S.; Chekmenev, E. Y. Microtesla SABRE Enables 10% Nitrogen-15 Nuclear Spin Polarization. *J Am Chem Soc* **2015**, *137* (4). <https://doi.org/10.1021/ja512242d>.
- (70) Zhou, Z.; Yu, J.; Colell, J. F. P.; Laasner, R.; Logan, A.; Barskiy, D. A.; Shchepin, R. V.; Chekmenev, E. Y.; Blum, V.; Warren, W. S.; Theis, T. Long-Lived  $^{13}\text{C}$  Nuclear Spin States Hyperpolarized by Parahydrogen in Reversible Exchange at Microtesla Fields. *Journal of Physical Chemistry Letters* **2017**, *8* (13). <https://doi.org/10.1021/acs.jpcclett.7b00987>.
- (71) Fekete, M.; Ahwal, F.; Duckett, S. B.; Duckett, S. B. Remarkable Levels of  $^{15}\text{N}$  Polarization Delivered through SABRE into Unlabeled Pyridine, Pyrazine, or Metronidazole Enable Single Scan NMR Quantification at the MM Level. *Journal of Physical Chemistry B* **2020**, *124* (22), 4573–4580. <https://doi.org/10.1021/acs.jpccb.0c02583>.
- (72) Shchepin, R. V.; Birchall, J. R.; Chukanov, N. V.; Kovtunov, K. V.; Koptug, I. V.; Theis, T.; Warren, W. S.; Gelovani, J. G.; Goodson, B. M.; Shokouhi, S.; Rosen, M. S.; Yen, Y.-F.; Pham, W.; Chekmenev, E. Y. Hyperpolarizing Concentrated Metronidazole  $^{15}\text{NO}$  Group over Six Chemical Bonds with More than 15 % Polarization and a 20 Minute Lifetime. *Chemistry - A European Journal* **2019**, *25* (37). <https://doi.org/10.1002/chem.201901192>.
- (73) Colell, J. F. P.; Emondts, M.; Logan, A. W. J.; Shen, K.; Bae, J.; Shchepin, R. V.; Ortiz, G. X.; Spanning, P.; Wang, Q.; Malcolmson, S. J.; Chekmenev, E. Y.; Feiters, M. C.; Rutjes, F. P. J. T.; Blümich, B.; Theis, T.; Warren, W. S. Direct Hyperpolarization of Nitrogen-15 in Aqueous Media with Parahydrogen in Reversible Exchange. *J. Am. Chem. Soc.* **2017**, *139* (23), 7761–7767. <https://doi.org/10.1021/jacs.7b00569>.
- (74) Theis, T.; Ortiz, G. X.; Logan, A. W. J.; Claytor, K. E.; Feng, Y.; Huhn, W. P.; Blum, V.; Malcolmson, S. J.; Chekmenev, E. Y.; Wang, Q.; Warren, W. S. Direct and Cost-Efficient Hyperpolarization of Long-Lived Nuclear Spin States on Universal  $^{15}\text{N}_2$ -Diazirine Molecular Tags. *Sci. Adv.* **2016**, *2* (3), e1501438. <https://doi.org/10.1126/sciadv.1501438>.
- (75) Shchepin, R.; Jaigirdar, L.; Theis, T.; Warren, W.; Goodson, B.; Chekmenev, E. Spin Relays Enable Efficient Long-Range Heteronuclear Signal Amplification by Reversible Exchange. *The Journal of Physical Chemistry C* **2017**, *121* (51), 28425–28434. <https://doi.org/10.1021/acs.jpcc.7b11485>.
- (76) Iali, W.; Roy, S. S.; Tickner, B. J.; Ahwal, F.; Kennerley, A. J.; Duckett, S. B. Hyperpolarising Pyruvate through Signal Amplification by Reversible Exchange (SABRE). *Angewandte Chemie - International Edition* **2019**, *58* (30), 10271–10275. <https://doi.org/10.1002/anie.201905483>.
- (77) Tickner, Ben. J.; Semenova, O.; Iali, W.; Rayner, P. J.; Whitwood, A. C.; Duckett, S. B. Optimisation of Pyruvate Hyperpolarisation Using SABRE by Tuning the Active Magnetisation Transfer Catalyst. *Catal Sci Technol* **2020**, *10* (5), 1343–1355. <https://doi.org/10.1039/C9CY02498K>.
- (78) Tomhon, P.; Abdulmojeed, M.; Adelabu, I.; Nantogma, S.; Kabir, M. S. H.; Lehmkuhl, S.; Chekmenev, E. Y.; Theis, T. Temperature Cycling Enables Efficient  $^{13}\text{C}$  SABRE-SHEATH Hyperpolarization and Imaging of  $[1-^{13}\text{C}]$ -Pyruvate. *J Am Chem Soc* **2022**, *144* (1). <https://doi.org/10.1021/jacs.1c09581>.

- (79) Adelabu, I.; TomHon, P.; Kabir, M. S. H.; Nantogma, S.; Abdulmojeed, M.; Mandzhieva, I.; Ettedgui, J.; Swenson, R. E.; Krishna, M. C.; Theis, T.; Goodson, B. M.; Chekmenev, E. Y. Order-Unity  $^{13}\text{C}$  Nuclear Polarization of  $[1-^{13}\text{C}]$ Pyruvate in Seconds and the Interplay of Water and SABRE Enhancement. *ChemPhysChem* **2022**, *23* (2), e202100839. <https://doi.org/10.1002/CPHC.202100839>.
- (80) Lindale, J. R.; Eriksson, S. L.; Tanner, C. P. N.; Zhou, Z.; Colell, J. F. P.; Zhang, G.; Bae, J.; Chekmenev, E. Y.; Theis, T.; Warren, W. S. Unveiling Coherently Driven Hyperpolarization Dynamics in Signal Amplification by Reversible Exchange. *Nat Commun* **2019**, *10* (1). <https://doi.org/10.1038/s41467-019-08298-8>.
- (81) Nantogma, S.; Eriksson, S. L.; Adelabu, I.; Mandzhieva, I.; Browning, A.; TomHon, P.; Warren, W. S.; Theis, T.; Goodson, B. M.; Chekmenev, E. Y. Interplay of Near-Zero-Field Dephasing, Rephasing, and Relaxation Dynamics and  $[1-^{13}\text{C}]$ Pyruvate Polarization Transfer Efficiency in Pulsed SABRE-SHEATH. *Journal of Physical Chemistry A* **2022**, *126* (48). <https://doi.org/10.1021/acs.jpca.2c07150>.
- (82) Theis, T.; Ariyasingha, N. M.; Shchepin, R. V.; Lindale, J. R.; Warren, W. S.; Chekmenev, E. Y. Quasi-Resonance Signal Amplification by Reversible Exchange. *Journal of Physical Chemistry Letters* **2018**, *9* (20). <https://doi.org/10.1021/acs.jpcclett.8b02669>.
- (83) Ariyasingha, N. M.; Lindale, J. R.; Eriksson, S. L.; Clark, G. P.; Theis, T.; Shchepin, R. V.; Chukanov, N. V.; Kovtunov, K. V.; Koptyug, I. V.; Warren, W. S.; Chekmenev, E. Y. Quasi-Resonance Fluorine-19 Signal Amplification by Reversible Exchange. *Journal of Physical Chemistry Letters* **2019**, *10* (15). <https://doi.org/10.1021/acs.jpcclett.9b01505>.
- (84) Sarracanie, M.; LaPierre, C. D.; Salameh, N.; Waddington, D. E. J.; Witzel, T.; Rosen, M. S. Low-Cost High-Performance MRI. *Sci. Rep.* **2015**, *5*, 15177. <https://doi.org/10.1038/srep15177>.
- (85) Cho, A. MRI for All. *Science* **2023**, *379* (6634), 748–751. <https://doi.org/10.1126/SCIENCE.ADH2295>.
- (86) Lehmkühl, S.; Suefke, M.; Kentner, A.; Yen, Y. F.; Blümich, B.; Rosen, M. S.; Appelt, S.; Theis, T. SABRE Polarized Low Field Rare-Spin Spectroscopy. *Journal of Chemical Physics* **2020**, *152* (18), 1–9. <https://doi.org/10.1063/5.0002412>.
- (87) Prabhat, A. M.; Crawford, A. L.; Mazurek, M. H.; Yuen, M. M.; Chavva, I. R.; Ward, A.; Hofmann, W. V.; Timario, N.; Qualls, S. R.; Helland, J.; Wira, C.; Sze, G.; Rosen, M. S.; Kimberly, W. T.; Sheth, K. N. Methodology for Low-Field, Portable Magnetic Resonance Neuroimaging at the Bedside. *Front Neurol* **2021**, *12*, 2191. <https://doi.org/10.3389/FNEUR.2021.760321/BIBTEX>.
- (88) Iglesias, J. E.; Schleicher, R.; Laguna, S.; Billot, B.; Schaefer, P.; McKaig, B.; Goldstein, J. N.; Sheth, K. N.; Rosen, M. S.; Kimberly, W. T. Quantitative Brain Morphometry of Portable Low-Field-Strength MRI Using Super-Resolution Machine Learning. *Radiology* **2022**. <https://doi.org/10.1148/radiol.220522>.
- (89) Cowley, M. J.; Adams, R. W.; Atkinson, K. D.; Cockett, M. C. R.; Duckett, S. B.; Green, G. G. R.; Lohman, J. A. B.; Kerssebaum, R.; Kilgour, D.; Mewis, R. E. Iridium N-Heterocyclic Carbene Complexes as Efficient Catalysts for Magnetization Transfer from Para -Hydrogen. *J Am Chem Soc* **2011**, *133* (16), 6134–6137. <https://doi.org/10.1021/ja200299u>.

- (90) Vazquez-Serrano, L. D.; Owens, B. T.; Buriak, J. M. The Search for New Hydrogenation Catalyst Motifs Based on N-Heterocyclic Carbene Ligands. *Inorg. Chim. Acta* **2006**, *359* (9), 2786–2797. <https://doi.org/10.1016/j.ica.2005.10.049>.
- (91) Kohler, S. J.; Yen, Y.; Wolber, J.; Chen, A. P.; Albers, M. J.; Bok, R.; Zhang, V.; Tropp, J.; Nelson, S.; Vigneron, D. B.; Kurhanewicz, J.; Hurd, R. E. In Vivo <sup>13</sup>C Carbon Metabolic Imaging at 3T with Hyperpolarized <sup>13</sup>C-1-Pyruvate. *Magn Reson Med* **2007**, *58* (1), 65–69. <https://doi.org/10.1002/mrm.21253>.
- (92) Park, J. M.; Recht, L. D.; Josan, S.; Merchant, M.; Jang, T.; Yen, Y. F.; Hurd, R. E.; Spielman, D. M.; Mayer, D. Metabolic Response of Glioma to Dichloroacetate Measured in Vivo by Hyperpolarized <sup>13</sup>C Magnetic Resonance Spectroscopic Imaging. *Neuro Oncol* **2013**, *15* (4). <https://doi.org/10.1093/neuonc/nos319>.
- (93) Hyppönen, V.; Stenroos, P.; Nivajärvi, R.; Ardenkjær-Larsen, J. H.; Gröhn, O.; Paasonen, J.; Kettunen, M. I. Metabolism of Hyperpolarised [1-<sup>13</sup>C]Pyruvate in Awake and Anaesthetised Rat Brains. *NMR Biomed* **2022**, *35* (2). <https://doi.org/10.1002/nbm.4635>.
- (94) Yen, Y. F.; Roux, P. Le; Mayer, D.; King, R.; Spielman, D.; Tropp, J.; Pauly, K. B.; Pfefferbaum, A.; Vasanawala, S.; Hurd, R. T2 Relaxation Times of <sup>13</sup>C Metabolites in a Rat Hepatocellular Carcinoma Model Measured in Vivo Using <sup>13</sup>C-MRS of Hyperpolarized [1-<sup>13</sup>C]Pyruvate. *NMR Biomed* **2010**, *23* (4). <https://doi.org/10.1002/nbm.1481>.
- (95) Liu, X.; Tang, S.; Mu, C.; Qin, H.; Cui, D.; Lai, Y.-C.; Riselli, A. M.; Delos Santos, R.; Carvajal, L.; Gebrezgiabhier, D.; Bok, R. A.; Chen, H.-Y.; Flavell, R. R.; Gordon, J. W.; Vigneron, D. B.; Kurhanewicz, J.; Larson, P. E. Z. Development of Specialized Magnetic Resonance Acquisition Techniques for Human Hyperpolarized [<sup>13</sup>C,<sup>15</sup>N<sub>2</sub>]Urea + [1-<sup>13</sup>C]Pyruvate Simultaneous Perfusion and Metabolic Imaging. *Magn Reson Med* **2022**, *88* (3), 1039–1054. <https://doi.org/https://doi.org/10.1002/mrm.29266>.
- (96) Dorokhov, Y. L.; Shindyapina, A. V.; Sheshukova, E. V.; Komarova, T. V. Metabolic Methanol: Molecular Pathways and Physiological Roles. *Physiol Rev* **2015**, *95* (2), 603–644. <https://doi.org/doi.org/10.1152/physrev.00034.2014>.
- (97) Skrzydlewska, E. Toxicological and Metabolic Consequences of Methanol Poisoning. <http://dx.doi.org/10.1080/713857189> **2008**, *13* (4), 277–293. <https://doi.org/10.1080/713857189>.
- (98) Schmidt, A. B.; De Maissin, H.; Adelabu, I.; Nantogma, S.; Etedgui, J.; Tomhon, P.; Goodson, B. M.; Theis, T.; Chekmenev, E. Y. Catalyst-Free Aqueous Hyperpolarized [1-<sup>13</sup>C]Pyruvate Obtained by Re-Dissolution Signal Amplification by Reversible Exchange. *ACS Sens* **2022**, *7* (11), 3430–3439. <https://doi.org/doi.org/10.1021/acssensors.2c01715>.
- (99) Hundshammer, C.; Braeuer, M.; Müller, C. A.; Hansen, A. E.; Schillmaier, M.; Düwel, S.; Feuerecker, B.; Glaser, S. J.; Haase, A.; Weichert, W.; Steiger, K.; Cabello, J.; Schilling, F.; Hövener, J. B.; Kjær, A.; Nekolla, S. G.; Schwaiger, M. Simultaneous Characterization of Tumor Cellularity and the Warburg Effect with PET, MRI and Hyperpolarized <sup>13</sup>C-MRSI. *Theranostics* **2018**, *8* (17), 4765–4780. <https://doi.org/10.7150/THNO.25162>.
- (100) Scroggins, B. T.; Matsuo, M.; White, A. O.; Saito, K.; Munasinghe, J. P.; Sourbier, C.; Yamamoto, K.; Diaz, V.; Takakusagi, Y.; Ichikawa, K.; Mitchell, J. B.; Krishna, M. C.; Citrin, D. E. Hyperpolarized [1-<sup>13</sup>C]-Pyruvate Magnetic Resonance Spectroscopic Imaging of Prostate

- Cancer In Vivo Predicts Efficacy of Targeting the Warburg Effect. *Clinical Cancer Research* **2018**, *24* (13), 3137–3148. <https://doi.org/10.1158/1078-0432.CCR-17-1957>.
- (101) Liberti, M. V.; Locasale, J. W. The Warburg Effect: How Does It Benefit Cancer Cells? *Trends Biochem Sci* **2016**, *41* (3), 211–218. <https://doi.org/10.1016/j.tibs.2015.12.001>.
- (102) Warburg, O. Über Den Stoffwechsel Der Carcinomzelle. *Naturwissenschaften* **1924**, *12* (50). <https://doi.org/10.1007/BF01504608>.
- (103) Albers, M. J.; Bok, R.; Chen, A. P.; Cunningham, C. H.; Zierhut, M. L.; Zhang, V. Y.; Kohler, S. J.; Tropp, J.; Hurd, R. E.; Yen, Y.-F. F.; Nelson, S. J.; Vigneron, D. B.; Kurhanewicz, J. Hyperpolarized <sup>13</sup>C Lactate, Pyruvate, and Alanine: Noninvasive Biomarkers for Prostate Cancer Detection and Grading. *Cancer Res.* **2008**, *68* (20), 8607–8615. <https://doi.org/10.1158/0008-5472.CAN-08-0749>.